

1 **Turbidity maximum zone index: A novel model for remote**
2 **extraction of turbidity maximum zone in different estuaries**

3 Chongyang Wang^{1‡}, Li Wang^{1‡}, Danni Wang², Dan Li^{1,3}, Chenghu Zhou^{1,3,4}, Hao
4 Jiang^{1,3}, Qiong Zheng¹, Shuisen Chen¹, Kai Jia¹, Yangxiaoyue Liu^{1,3}, Ji Yang^{1,3}, Xia
5 Zhou¹ and Yong Li^{1,3}

6 ¹ Guangdong Open Laboratory of Geospatial Information Technology and Application, Key Lab of
7 Guangdong for Utilization of Remote Sensing and Geographical Information System, Guangzhou
8 Institute of Geography, Guangdong Academy of Sciences, Guangzhou 510070, China

9 ² Guangzhou Xinhua University, Guangzhou 510520, China

10 ³ Southern Marine Science and Engineering Guangdong Laboratory (Guangzhou), Guangzhou
11 511458, China

12 ⁴ State Key Laboratory of Resources and Environmental Information System, Institute of
13 Geographic Sciences and Natural Resources Research, Chinese Academy of Sciences, Beijing
14 100101, China

15 ‡ Equally contributed to this work

16 **Correspondence:** Dan Li (lidan@gdas.ac.cn); Chenghu Zhou (zhouch@reis.ac.cn)

17 **Abstract.** An efficient recognition and extraction of the estuarine turbidity maximum
18 zone (TMZ) is important for studying terrestrial hydrological processes. Although
19 many studies relevant to TMZ have been conducted worldwide, the extraction methods
20 and criteria used to describe TMZ vary significantly both spatially and temporally. To
21 improve the applicability of the methods adopted in previous studies and to develop a

22 novel model to accurately extract TMZ in multiple estuaries and different seasons from
23 remote sensing imageries, this study estimated the total suspended solids (TSS) and
24 chlorophyll a (Chla) concentrations in three estuaries. These were the Pearl River
25 Estuary (PRE), the Hanjiang River Estuary (HRE), and the Moyangjiang River Estuary
26 (MRE) of Guangdong Province, China. The spatial distribution characteristics of the
27 TSS and Chla concentrations were analyzed. A nearly opposite association was found
28 between the TSS and Chla concentrations in the three estuaries, particularly in the PRE.
29 The regions with high (low) TSS concentrations had relatively low (high) Chla
30 concentrations and therefore, a turbidity maximum zone index (TMZI), defined as the
31 ratio of the difference and sum of the logarithmic transformation of the TSS and Chla
32 concentrations, was firstly proposed. By calculating the TMZI values in the PRE on
33 November 20, 2004 (low-flow season), it was found that the criterion ($TMZI > 0.2$)
34 could be used to identify the TMZs of the PRE effectively. The TMZ extraction results
35 were generally consistent with the visual interpretation results. The area-based accuracy
36 measures showed that the quality (Q) of the extraction reached 0.8429. The same
37 criterion was applied in the PRE on October 18, 2015 (high-flow season), and high
38 accuracy and consistency across seasons were observed ($Q = 0.8171$). The western
39 shoal of the PRE was the main distribution area of TMZs. Extracting TMZs by the
40 newly proposed index performed well in different estuaries and on different dates (HRE
41 on August 13, 2008 in the high-flow season and MRE on December 6, 2013 in the low-
42 flow season). Compared to the previous fixed threshold of TSS or turbidity methods,

43 extracting TMZ using TMZI had higher accuracy and better applicability (Q: 0.1046–
44 0.4770 vs. 0.8171–0.8429). Evidently, this unified TMZI is potentially an optimized
45 method for the global monitoring and extraction of TMZs of estuaries from different
46 satellite remote sensing imageries. It can be used to help the understanding of the spatial
47 and temporal variation of TMZs and estuarine processes at regional and global scales,
48 as well as improve the management and sustainable development of regional society
49 and the natural environment.

50 Keywords: turbidity maximum zone; turbidity maximum zone index; total suspended
51 solid; chlorophyll a; remote sensing; estuary

52 **1 Introduction**

53 The turbidity maximum zone (TMZ) is the dynamic turbid water area within an
54 estuary, where the suspended solid concentrations, namely, sediment and matter, are
55 consistently and significantly higher than landward and seaward ([Shen, 1995](#); [Gebhardt
56 et al., 2005](#); [Yu et al., 2014](#); [Li et al., 2019](#)). It is a special phenomenon of suspended
57 sediment movement and migration in estuaries worldwide ([Schubel, 1968](#); [Shi et al.,
58 1993](#); [Mitchell et al., 2012](#); [Wang et al., 2021](#)). The spatial distributions and dynamic
59 changes of TMZs not only have a deep and wide impact on the formation and
60 development of estuary morphology, channels, shoals, and sandbars ([Asp et al., 2018](#);
61 [Azhikodan and Yokoyama, 2019](#); [Li et al., 2019](#)), but also significantly affect the
62 physics and geochemical and biogeochemical processes of natural estuarine

63 environments, as well as social production activities ([Gebhardt et al., 2005](#); [Jalón-Rojas](#)
64 [et al., 2016](#); [Kitheka et al., 2016](#); [Toublanc et al., 2016](#); [Yan et al., 2020](#)). TMZ has long
65 been a popular area for scientific study and engineering innovations among researchers,
66 government agencies, engineering corporations, and communities ([Shen et al., 2001](#);
67 [Shi et al., 2017](#); [Jiang et al., 2019](#); [Wang et al. 2021](#)).

68 Previous studies have examined TMZ from various aspects based on different data
69 resources and methods, such as the characteristics and dynamics of total suspended
70 solids (TSS) concentrations in TMZ ([Yang et al., 2014](#); [Wan and Wang, 2017](#); [Grasso](#)
71 [et al., 2018](#)), the mechanisms and formation of TMZ ([Brenon and Hir, 1999](#); [Wai et al.,](#)
72 [2004](#); [Yu et al., 2014](#); [Toublanc et al., 2016](#)), the location, distribution, and change of
73 TMZ across time ([Jiang et al., 2013](#); [Jalón-Rojas et al., 2016](#); [Li et al., 2019](#); [Yan et al.,](#)
74 [2020](#)), the interaction with other factors, and its long-term trend ([Gebhardt et al., 2005](#);
75 [Chen et al., 2016](#); [Li et al., 2019](#)). The location of TMZ in an estuary is a fundamental
76 question and an important aspect of studying TMZ. It was found that there were two
77 major ways to obtain the locations and distributions of TMZs ([Wang et al., 2021](#)). One
78 was a relatively approximate description, such as TMZ locations corresponding to the
79 front of the salinity wedge and moving range of stagnation points, or a distance from
80 coastlines ([Feng et al., 2002](#); [Mitchell, 2013](#); [Kitheka et al., 2016](#); [Liu et al., 2016](#);
81 [Toublanc et al., 2016](#); [Gong et al., 2017](#); [Zhang et al., 2019](#); [Yan et al., 2020](#)). The other
82 was a relatively quantitative result. The thresholds of TSS concentrations or turbidity
83 criteria were used to extract the distribution of TMZs ([Jiang et al., 2013](#); [Yang and Liu,](#)

84 [2015; Chen et al., 2016; Jalón-Rojas et al., 2016; Shi et al., 2017; Li et al., 2019](#)).
85 However, the fixed threshold method has potential drawbacks. It is a challenging task
86 to precisely generate TMZ extraction results at different times using a fixed threshold
87 of TSS concentration because TSS concentrations showed significant variations in
88 different seasons. Moreover, the threshold values are difficult to transfer from local
89 regions to other regions because research and a scientific basis are lacking. The
90 threshold method and criteria vary significantly in different estuaries, in different
91 regions of the same estuary, in the same estuary at different times, and by different
92 studies, demonstrating considerable subjectivity. The results were not comparable
93 ([Wang et al., 2021](#)).

94 TSS concentrations in the TMZs and adjacent waters vary significantly ([Uncles et](#)
95 [al., 2000; Park et al., 2008; Mitchell, 2013; Wang et al., 2018](#)). Many studies have
96 shown that suspended solids can affect the growth of chlorophyll a (Chla) through
97 absorption and sunlight scattering in water ([Pozdnyakov et al., 2005; Chen et al., 2015;](#)
98 [Montanher et al., 2014; Wang et al., 2017a; Wang et al., 2020b](#)). Therefore, it was
99 concluded that there is a relationship between TSS concentrations and Chla
100 concentrations and different characteristics in TMZ and normal water bodies in
101 estuaries. This relationship might be used to overcome the drawbacks of previous
102 methods of extracting TMZ and distinguish and recognize TMZ effectively.

103 Based on this analysis, the objectives of this study are to propose a new model
104 with better adaptability and robustness for distinguishing and extracting TMZ in

105 different estuaries and in different seasons. To achieve this goal, the TSS and Chla
106 concentrations in the Pearl River Estuary (PRE), Hanjiang River Estuary (HRE), and
107 Moyangjiang River Estuary (MRE) were first estimated. The different spatial
108 characteristics were analyzed and compared. Subsequently, the corresponding
109 relationship and special features of TSS and Chla concentrations were used to develop
110 a turbidity maximum zone index (TMZI). Finally, the TMZs in these estuaries were
111 extracted at different times by the model (TMZI) and validated and assessed for
112 accuracy.

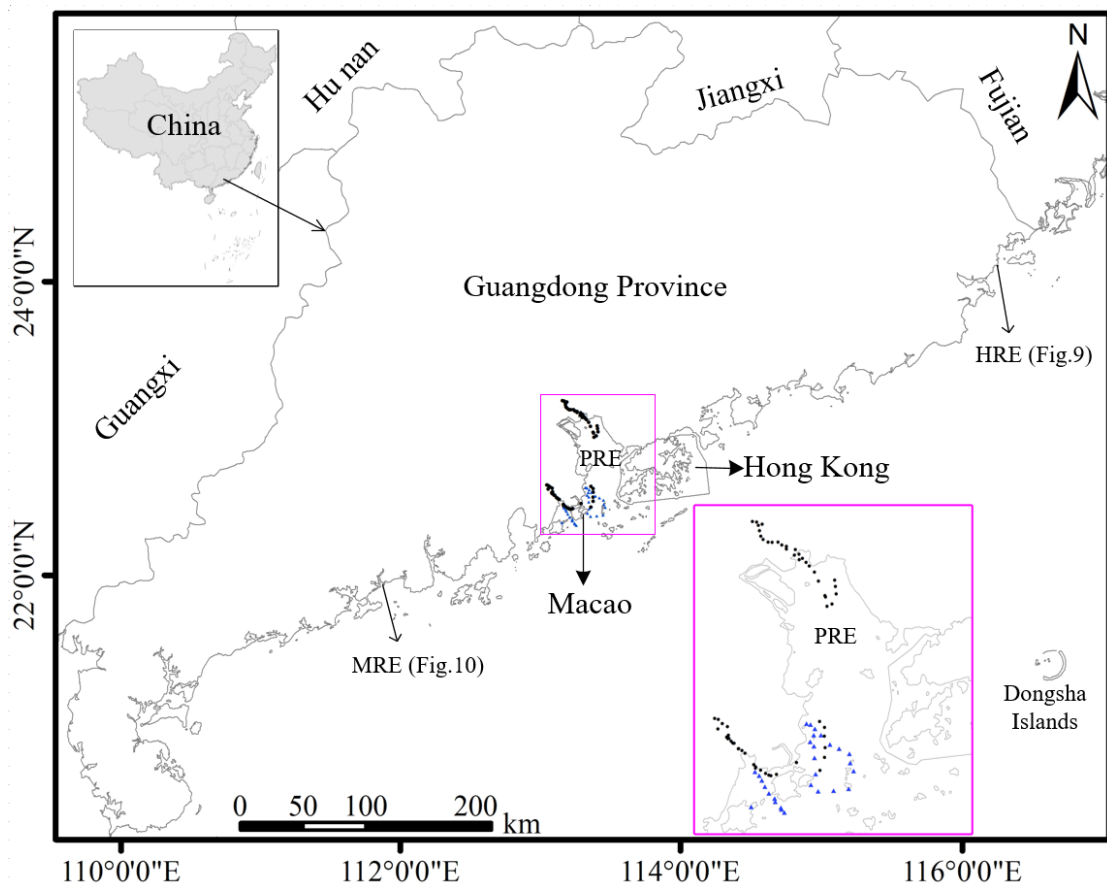
113 The remainder of this paper is organized as follows. The study areas, in situ data,
114 satellite imagery, TSS concentration data, Chla retrieval model, and its calibration and
115 validation are described in [Section 2](#), as well as the TMZ extraction accuracy
116 assessment measures. The spatial analysis of TSS concentration, Chla concentration,
117 and the corresponding relationship between them are presented in [Section 3.1](#). The
118 establishment of TMZI and its application and assessment in different estuaries and at
119 different times are shown in [Sections 3.2-3.5](#). The summary and conclusions are
120 presented in [Section 4](#).

121 **2 Dataset and methods**

122 **2.1 Study areas**

123 The study areas include the Pearl, Hanjiang, and Moyangjiang River Estuaries of
124 Guangdong Province, South China ([Figs. 1, 4, and 7-10](#)). The PRE (horn-shaped) is

125 located between longitudes 113.45 °114.2 °E and latitudes 22.25 °22.85 °N, mainly in
 126 the core zone of Guangdong-Hong Kong-Macao Greater Bay Area. The HRE (forking-
 127 shaped) is located between longitudes 116.6 °117 °E and latitudes 23.2 °23.6 °N, mainly
 128 in Shantou city, Eastern Guangdong Province. The MRE (calabash-shaped) is located
 129 between longitudes 111.9 °112.3 °E and latitudes 21.66 °21.8 °N, mainly in Yangjiang
 130 city, Western Guangdong Province.



131
 132 **Fig. 1.** Study areas (PRE, HRE, and MRE) and the locations of the in-situ data indicated by black
 133 dots and blue triangles.

134 The Pearl River has the second largest annual runoff and is the third largest river
 135 in China. The Hanjiang and Moyangjiang Rivers are the second and third largest rivers
 136 in Guangdong Province (Chen et al., 2011; Wang et al., 2018; Wang et al., 2020a).

137 Previous studies have reported that the sediment loads of the Pearl, Hanjing and
138 Moyangjiang Rivers were $7.53 \cdot 10^7$, $6.93 \cdot 10^6$ and $3.27 \cdot 10^5$ ton per year, respectively
139 (Wang et al., 2017a, b; Wang et al., 2020a). It was found that the three rivers and
140 estuaries have different characteristics, and much associated research has been
141 conducted in these regions for a long time.

142 **2.2 In-situ and satellite data**

143 The 89 in-situ samples, including water surface reflectance and Chla
144 concentrations, were collected from the PRE (Fig. 1, Table 1). Sixty of these samples
145 were also used in a previous study by the current authors (black dots) (Chen et al., 2011).
146 The present study included 29 new samples (blue triangles). Here, these samples were
147 used to recalibrate and validate a Landsat-based Chla concentration retrieval model.

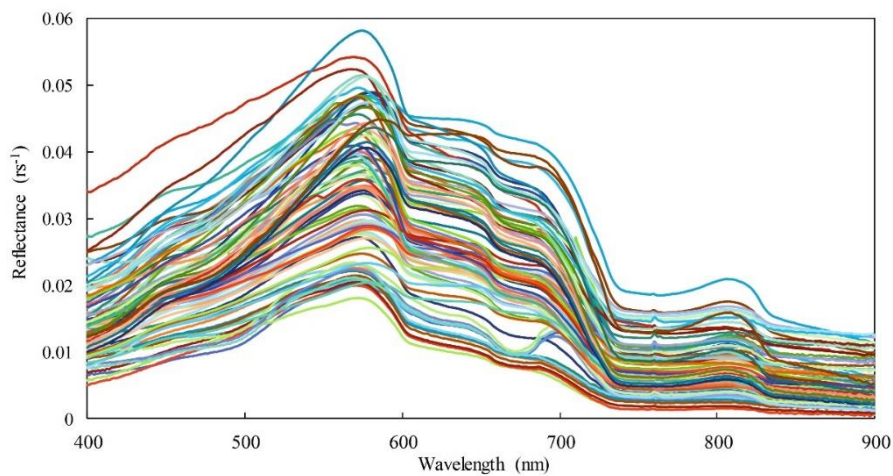
148 In addition, four scenes of good quality Landsat imageries were used. Two images
149 from TM and OLI (path/row = 122/44) were captured on November 20, 2004
150 (ProductID: LT05_L1TP_122044_20041120_20161129_01_T1), and October 18,
151 2015 (LC08_L1TP_122044_20151018_20170403_01_T1), respectively, covering the
152 PRE (Figs. 7a and 8c). The image from TM (path/row = 120/44) was captured on
153 August 13, 2008 (LT05_L1TP_120044_20080813_20161030_01_T1), covering the
154 HRE (Fig. 9c). The final image from OLI (path/row = 123/45), was captured on
155 December 6, 2013 (LC08_L1TP_123045_20131206_20170428_01_T1), covering the
156 MRE (Fig. 10c).

157 **Table 1**

158 The 89 in-situ data.

Date	Samples	Measurements	
Dec 9, 2006	16	Reflectance, Chla	
Dec 21, 2006	12	Reflectance, Chla	Same as
Dec 27, 2007	15	Reflectance, Chla	Chen et al. (2011)
Dec 31, 2007	17	Reflectance, Chla	
Nov 2, 2012	18	Reflectance, Chla	Newly added
Sep 10, 2013	11	Reflectance, Chla	

159



160

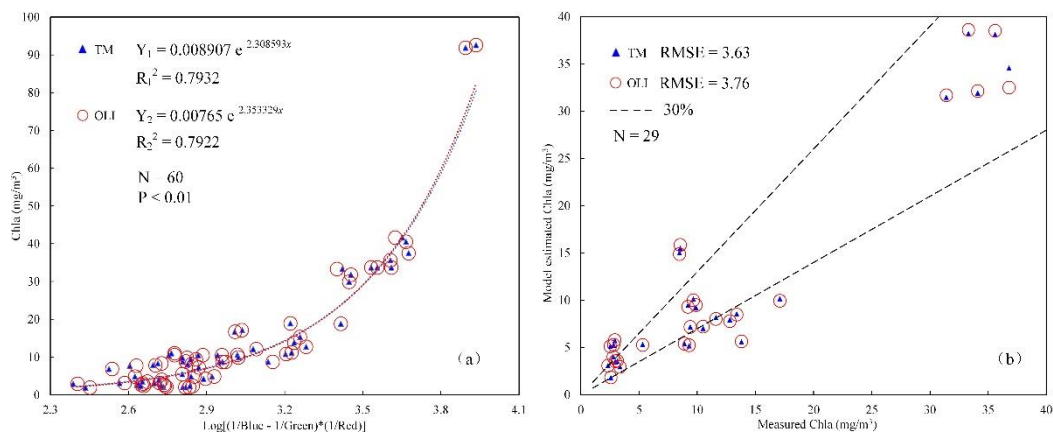
161 **Fig. 2.** Remote sensing reflectance of surface water of the 89 in situ data.

162 **2.3 Total suspended solids data and chlorophyll a data**

163 The aim of this study was to establish and develop a new model (TMZI) based on

164 TSS concentrations and Chla concentrations, and further extract TMZs in three

165 estuaries of Guangdong Province. Therefore, the TSS and Chla concentrations in the
 166 study areas were first calculated. The TSS concentration data were obtained from
 167 previous work of the current authors (Wang et al., 2017a, b; Wang et al., 2018; Wang et
 168 al., 2020a). The corresponding Chla data required retrieval using Landsat imagery.
 169 Consequently, a Landsat-based Chla concentration retrieval model was expected to be
 170 suitable for different estuaries. Many models have been developed to estimate Chla
 171 concentration from different remote sensing data (Gregg and Casey, 2004; Chen et al.,
 172 2011; Kim et al., 2016a, b; Attila et al., 2018). Following the features and forms of
 173 some typical chlorophyll a retrieval models (Le et al., 2009; Chen et al., 2011; Le et al.,
 174 2013; Song et al., 2013), a three-band Landsat-based chlorophyll a model using the 89
 175 in-situ samples was recalibrated and validated (Fig. 3; Equation 1). The model, based
 176 on Landsat TM and OLI sensors, explained approximately 80% of the Chla
 177 concentration variation (Chla: 1.92-92.6 mg/m³, N=60, P-value<0.01) and had an
 178 acceptable validation accuracy (Chla: 2.33-36.8 mg/m³, RMSE ≤ 3.76 mg/m³, N=29).



179
 180 **Fig. 3.** The calibration (a) and validation (b) results of the Chla retrieval models based on 89 in situ
 181 data for Landsat sensors.

182
$$Chla = a * e^{b * \text{Log}_{(10)}\left[\left(\frac{1}{R_1} - \frac{1}{R_2}\right) * \frac{1}{R_3}\right]} \quad (1)$$

183 where R_1 , R_2 and R_3 represent the blue, green, and red band of the TM and OLI
 184 sensors, respectively. The parameters a and b corresponding to the TM and OLI sensors
 185 are 0.008907, 2.308593 and 0.00765, 2.353329, respectively. The unit of chlorophyll a
 186 concentration is in mg/m^3 .

187 **2.4 Accuracy assessment measures**

188 To evaluate TMZI extraction accuracy and compare the performances of the
 189 different methods, the common accuracy measures of object recognition in remote
 190 sensing, area-based accuracy measures (Cai et al., 2018), was used.

191 Suppose that A_E is the area of the extracted TMZ, A_C is the correct part of A_E , and
 192 A_R is the reference TMZ. Then the quality (Q) of the TMZ extraction results in the study
 193 could be defined as follows (equation 2).

194
$$Q = \frac{A_C}{A_E + A_R - A_C} \quad (2)$$

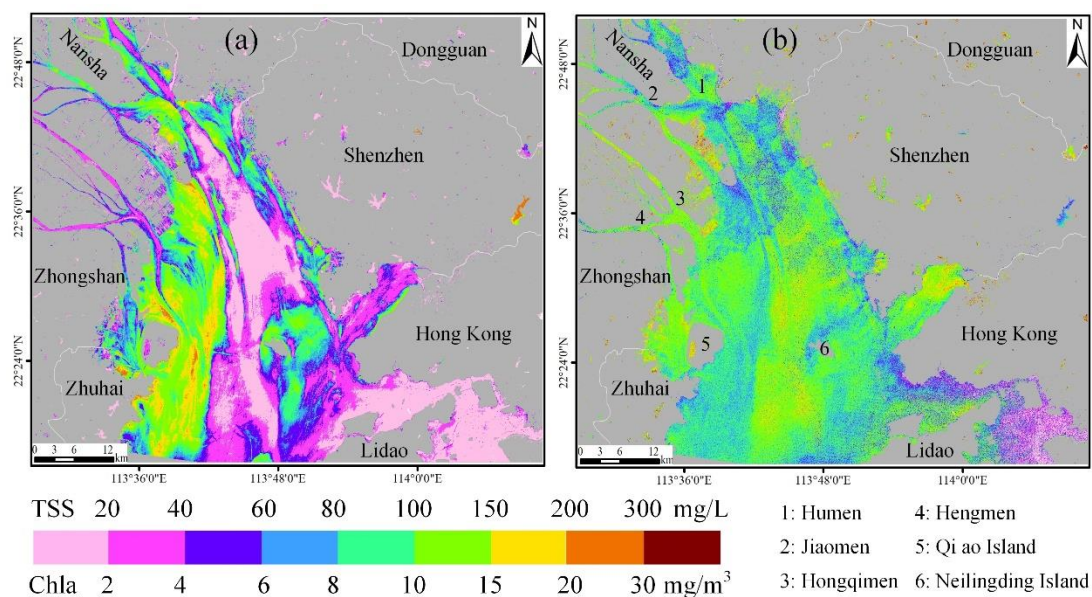
195 The range of Q is 0 to 1. The bigger the Q value, the higher the accuracy of the
 196 TMZ extraction results, and the better performance of the method.

197 **3 Results and discussion**

198 **3.1 The spatial characteristics of TSS and Chla concentrations in** 199 **estuaries**

200 Chla concentrations in each estuary were estimated using the Chla concentration
 201 retrieval model that was developed (Fig. 3). The different spatial distribution
 202 characteristics of the TSS and Chla concentrations were analyzed. Taking the PRE as

203 an example, TSS concentrations in the low-flow season of the PRE (November 20,
 204 2004) have a large variation ranging from 1.37 mg/L to more than 200 mg/L (Fig. 4a).
 205 Due to the strong interaction between runoff and tide, the main region of high TSS
 206 concentrations is in the west shoal of the PRE (Wang et al., 2018), where concentrations
 207 of more than 100 mg/L were frequently found. In addition, TSS concentrations in parts
 208 of the east shoal and Neilingding island adjacent waters were also relatively higher. The
 209 other areas of the PRE have low TSS concentrations, where the maximum value is
 210 generally not more than 40 mg/L, particularly in the Hong Kong coastal water bodies
 211 (Fig. 4a).



212
 213 **Fig. 4.** The estimated TSS concentrations (a) and Chla concentrations (b) in the PRE on November
 214 20, 2004.

215 In contrast to the TSS concentration results, the Chla concentrations in the PRE
 216 have significantly lower values of less than 20 mg/m³ in almost the entire PRE (Fig.
 217 4b). The results concord with the findings of Liu et al. (2017) and Huang et al. (2005),

218 who found that Chla concentrations ranged from 0.24 mg/m^3 to 21.5 mg/m^3 in the PRE
219 at different times. Furthermore, Chla concentrations in the PRE show almost opposite
220 spatial characteristics to TSS concentrations. Apart from the eastern Lidao district
221 coastal water bodies, the regions of relatively high (low) Chla concentrations are the
222 regions of relatively low (high) TSS concentrations. These corresponding features are
223 apparent in the four waterways, namely, Humen, Jiaomen, Hongqimen, and Hengmen
224 waterways and the shoals, and channels of the PRE (Fig. 4).

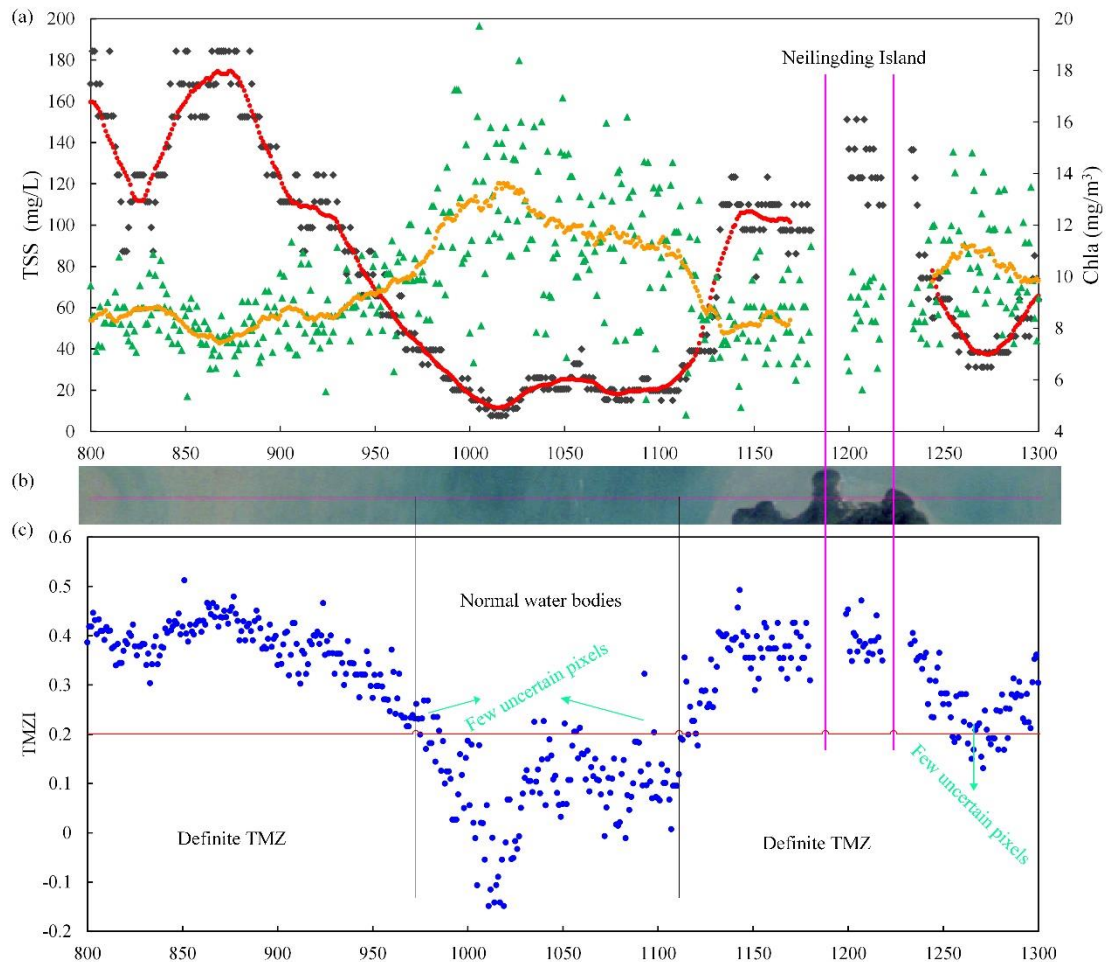
225 To further analyze and assess the corresponding relationship between TSS and
226 Chla concentrations in the estuaries, three rows of TSS and Chla concentration values
227 in the PRE were extracted (Fig. 7a; pink lines; rows 1200, 1600, and 1900, columns
228 from 800 to 1300). The results for row 1600 are shown in Fig. 5(a). A correlation
229 analysis showed a significant negative correlation between TSS and Chla
230 concentrations. For the original TSS and Chla concentrations, the correlation
231 coefficient was -0.6531. The correlation coefficient reaches approximately -0.9 for its
232 trend lines (Fig. 5a).

233 **3.2 Establishment and application of TMZI**

234 Based on the analysis and corresponding features between TSS and Chla
235 concentrations, it is considered that the transform results derived from the two water
236 color elements may help to better distinguish and extract TMZ. In this study, TMZI was
237 defined as the ratio of the difference and sum of logarithmic transformation of TSS

238 concentrations and Chla concentrations (equation 3), which is similar to the normalized
 239 difference vegetation index (NDVI).

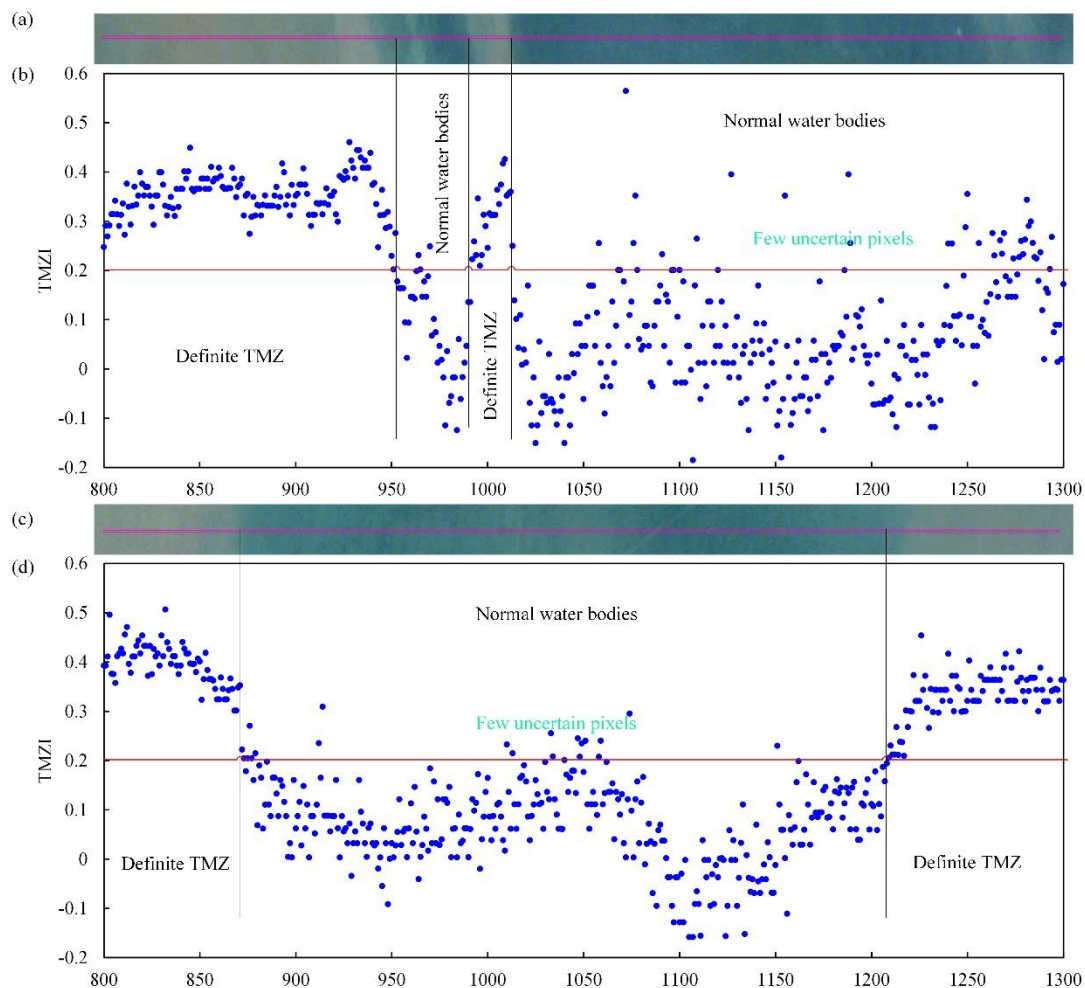
240
$$TMZI = [\text{Log}(TSS) - \text{Log}(Chla)] / [\text{Log}(TSS) + \text{Log}(Chla)] \quad (3)$$



241
 242 **Fig. 5.** The corresponding spatial relationship between the TSS concentrations, indicated by black
 243 dots and red trend line, and Chla concentrations, indicated by green triangles and orange trend line
 244 of row 1600 (a), the true color imagery (b) and the corresponding values of TMZI (c).

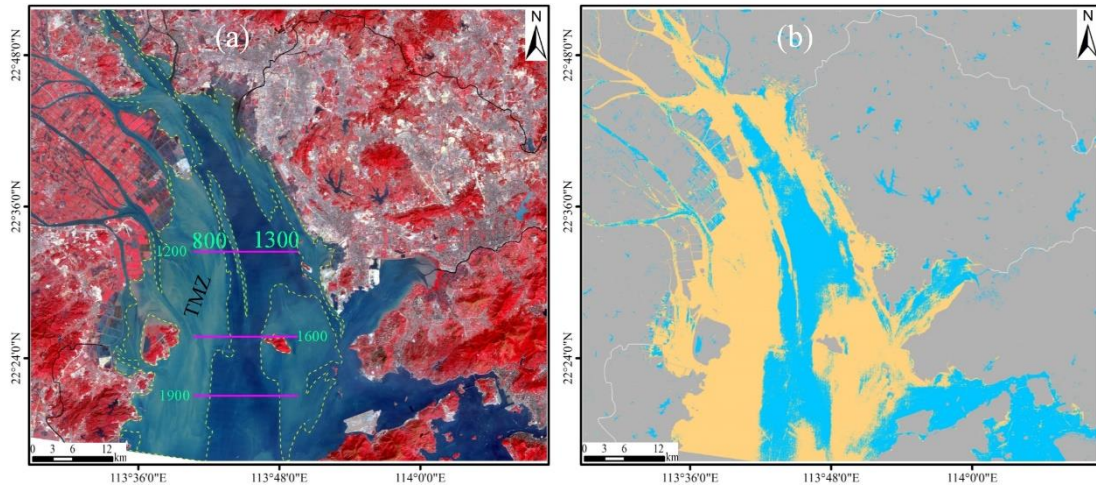
245 According to the definition and equation, this study calculated TMZI values (Figs.
 246 5c, 6b and d). Taking the results of row 1600 as an example (Fig. 5b and c), the row
 247 pixels can be mainly divided into one TMZ (columns 800-975), normal water bodies
 248 (columns 975-1110), and another TMZ (columns 1110-1300) from left to right. The null

249 values located in columns 1180-1200 and 1220-1235 are Neilingding Island (Figs. 5
 250 and 7a). Through a comparison with the results of TMZI, it is found that all the values
 251 of TMZI corresponding to TMZ pixels are larger than 0.2, while the values
 252 corresponding to normal water body pixels are all smaller than 0.2, except for a few
 253 blurry pixels (Figs. 5b and c). For the results of rows 1200 and 1900, similar
 254 corresponding characteristics between TMZ and TMZI and the same criterion were also
 255 found (Fig. 6). Therefore, TMZI showed a significant feature and had the potential to
 256 develop into a better model for recognizing and extracting estuarine TMZ.



257
 258 **Fig. 6.** The true color imagery and the corresponding values of TMZI of rows 1200 (a and b) and
 259 1900 (c and d).

260 The TMZI of the entire Landsat TM imagery was subsequently calculated, and
261 TMZs in the PRE were extracted. [Fig. 7\(b\)](#) shows the spatial distribution results of
262 TMZ in the PRE on November 20, 2004. TMZ is widely distributed throughout the
263 PRE, accounting for more than half of the water areas in the imagery. Among them, the
264 main TMZ is located within an average distance of 11 km from the Panyu, Nansha,
265 Zhongshang, and Zhuhai coasts, which approximately corresponds to the west shoal in
266 the PRE. In the western Dongguan and Shenzhen coastal water bodies, an
267 approximately rectangular TMZ develops approximately 5 km from the coastline,
268 which indicates the location of the east shoal of the PRE ([Wang et al., 2018](#)). In addition,
269 a third main TMZ in the PRE located from surrounding Neilingding Island to western
270 Hong Kong water bodies is found, although TSS concentrations in TMZ are lower than
271 those of the former TMZs ([Figs.4a and 7b](#)). Compared to the visual interpretation of
272 TMZ results in previous works by the current authors ([Fig.7 a](#)) ([Wang et al., 2020b,](#)
273 [2021](#)), the area-based accuracy measures show that the quality of extraction achieves
274 0.8429. The good TMZ extraction results and the high validation accuracy by TMZI in
275 this study indicate a more effective way to recognize TMZs in estuaries ([Figs. 6-7](#)).



276

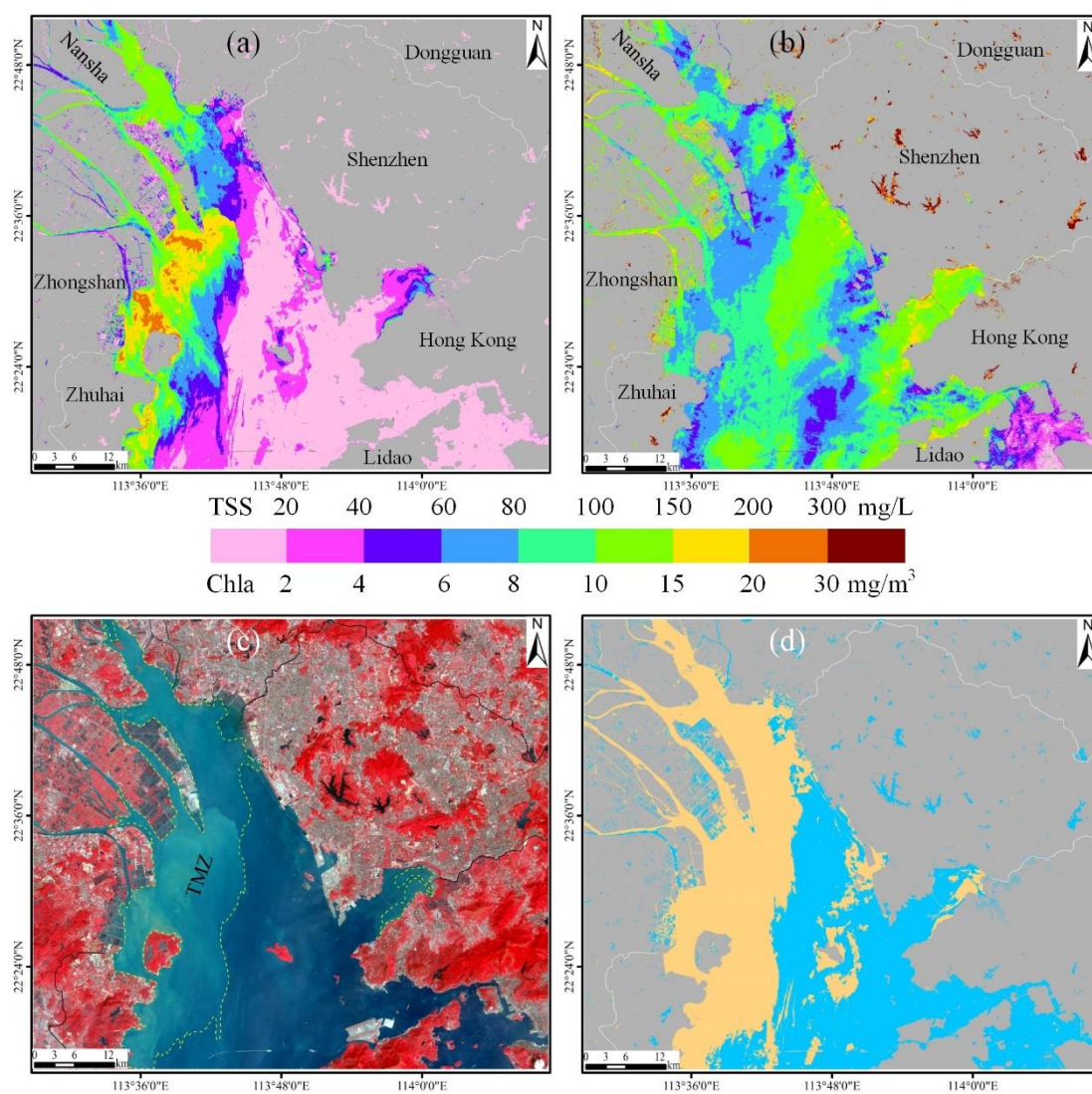
277 **Fig. 7.** False color imagery (USGS 1982; NASA 2001) and the visual interpretation TMZ results
 278 (regions indicated by yellow dashed frames) (Wang et al., 2020b, 2021) (a), and the extracted TMZ
 279 results, indicated by mango colors (b) in the PRE on November 20, 2004 (low-flow season).

280 3.3 Validation of the accuracy of TMZI in different seasons

281 Due to the complexity of hydrodynamic environments, the estuarine factors and
 282 water color elements show significant variations in different seasons, even in the same
 283 estuary at different times of the day. Therefore, this study further validated the accuracy
 284 of TMZI for extracting TMZ in the PRE during the high-flow season (October 18, 2015).

285 **Fig. 8(a)** and **(b)** demonstrate the retrieved TSS and Chla concentration results in
 286 the high-flow season of PRE. The results in different seasons are significantly different
 287 (**Figs. 4** and **8**). On October 18, 2015, TSS concentrations in the PRE had wider
 288 variables, ranging from 2.23 to 286.6 mg/L. However, the water bodies with high TSS
 289 concentrations (more than 80 mg/L) were mainly in the outlets of four waterways,
 290 namely, the Humen, Jiaomen, Hongqimen, and Hengmen waterways. The other regions

291 of the PRE have significantly lower TSS concentrations of generally less than 20 mg/L
 292 (Fig. 8a). Similar to the corresponding features between TSS and Chla concentrations
 293 in the low-flow season, the almost opposite spatial characteristics remain in the high-
 294 flow season. For regions with relatively high (low) Chla concentrations there are
 295 relatively low (high) TSS concentrations (Figs. 8a and b). Notably, the eastern Lidao
 296 district coastal water bodies are an exception, with the same results in the low-flow
 297 season (Fig. 4). Both TSS and Chla concentrations in the zone are relatively low (Figs.
 298 4 and 8).



299

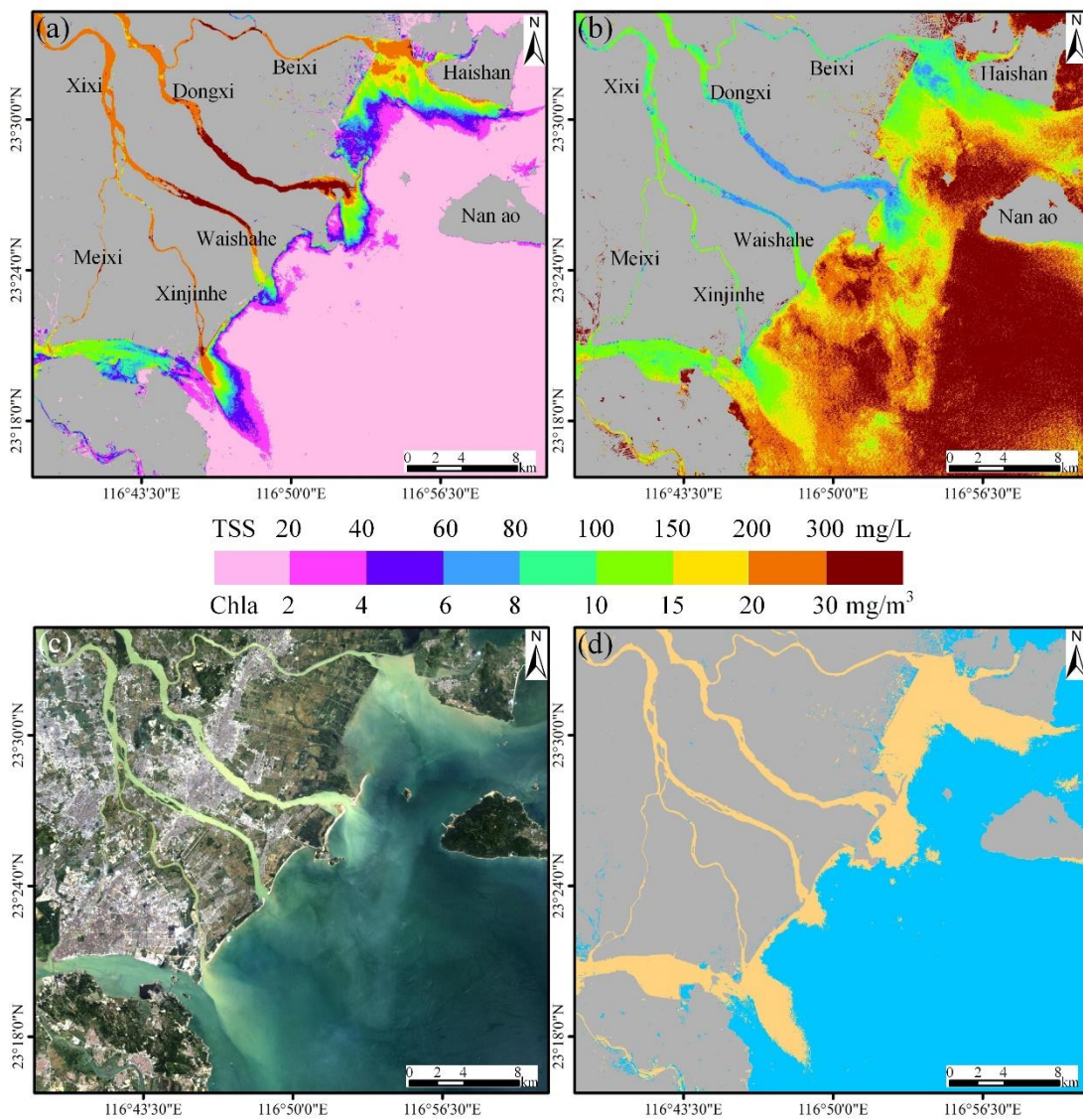
300 **Fig. 8.** The estimated TSS concentrations (a), Chla concentrations (b), false color imagery (USGS
301 1982; NASA 2001), and the visual interpretation TMZ results (regions indicated by yellow dashed
302 frames) (Wang et al., 2020b) (c), and extracted TMZ results, indicated by mango colors mango
303 colors (d) in the PRE on October 18, 2015 (high-flow season).

304 Using the results of TSS and Chla concentrations of the PRE on October 18, 2015,
305 the TMZI was calculated and TMZs of the PRE were extracted in the high-flow season
306 (Fig. 8d). Compared with the visual interpretation TMZ results (Fig.8 c) (Wang et al.,
307 2020b), the area-based accuracy measures show that the quality of extraction is 0.8171.
308 It is also indicated that an acceptable accuracy is obtained by TMZI in the high-flow
309 season of the PRE. In addition, only one main TMZ remains along the west coast of the
310 PRE (Fig. 8d), which is similar to one of the main TMZs in the low-flow season of
311 2004 (Fig. 7b). However, clear differences remain in different seasons, such as TMZs
312 in the Hongqimen and Hengmen waterways and the eastern Zhuhai coasts (Figs. 7b and
313 8d). The other TMZs in the high-flow season of 2015 are mainly located in the
314 surrounding Dachanwan Wharf of Shenzhen and Neilingding Island. The distributions
315 are less apparent than those in the low-flow season of 2004 (Fig. 7b). Besides, two
316 relatively small isolated TMZs can be found on the two artificial islands of the Hong
317 Kong-Zhuhai-Macao Bridge (Fig. 8d), which may imply the associated influence of
318 human activities.

319 According to the analysis of the PRE results on October 18, 2015, it is
320 demonstrated that the TMZI and the criterion ($TMZI > 0.2$) also perform well in
321 extracting estuarine TMZ in different seasons using Landsat OLI imagery.

322 3.4 Assessment of the applicability of TMZI in different estuaries

323 To further assess the applicability of TMZI in different estuaries, as for the PRE,
324 the corresponding TMZ results in the HRE and the MRE were also calculated and
325 validated.



326

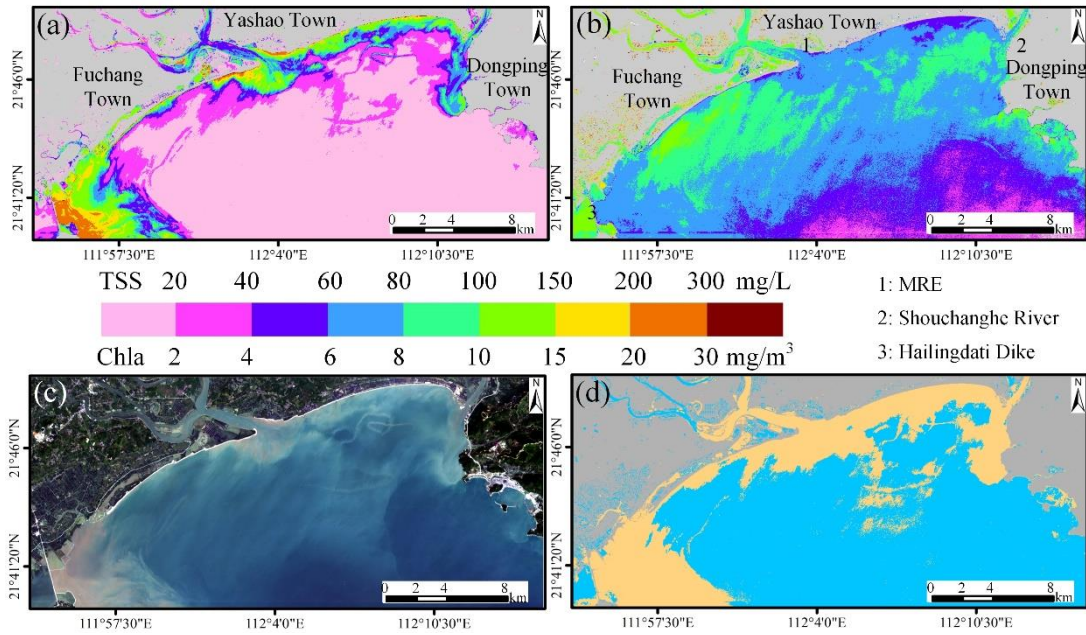
327 **Fig. 9.** The estimated TSS concentrations (a), Chla concentrations (b), true color imagery (USGS
328 1982; NASA 2001) (c), and extracted TMZ results, indicated by mango colors (d) in the HRE on
329 August 13, 2008 (high-flow season).

330 **Fig. 9** (a) and (b) indicate the results of TSS and Chla concentrations in the HRE
331 on August 13, 2008. The TSS concentrations downstream and in the estuary of the HRE
332 are significantly higher than the outer shelf area, particularly in the downstream of the
333 Dongxi River and Xinjinhe River waterways of the Hanjiang River, with a mean value
334 in excess of 300 mg/L (**Fig. 9a**). TSS concentrations in the offshore area (South China
335 Sea) are frequently less than 20 mg/L. Therefore, a significant decreasing trend of TSS
336 concentration is found from the northwest to southeast in the HRE (**Fig. 9a**).
337 Furthermore, the Chla concentrations in the HRE show opposite spatial distributions
338 characteristics, which resembles the findings in the PRE (**Figs. 4 and 8**). Relatively low
339 Chla concentrations are mainly generally found in the downstream and estuary, and the
340 outer shelf area has high values (**Fig. 9b**). The Chla concentrations in the HRE range
341 from 4.1 to 37.3 mg/m³ (**Fig. 9b**), which is slightly higher than that of the PRE (**Figs. 4**
342 **and 8**).

343 The TMZ extraction results for the HRE are shown in **Fig. 9(d)**. The TMZs are
344 distributed in all the downstream and estuaries of the Hangjiang River. They can be
345 divided into four main TMZs based on different waterways, namely, the Beixi, Dongxi,
346 Waishahe, Xinjinhe, and Meixi waterways of the Hanjing River. The maximum TMZ
347 is located within an average distance of 3 km from the Beixi estuary, western Haishan

348 coast, and the coastlines between the Beixi and Dongxi estuaries. The second largest
349 TMZ of the HRE is distributed from the Meixi to the Xinjinhe estuaries. The region of
350 the main TMZ of the Xinjinhe estuary appears knife-shaped, which is mainly caused
351 by the runoff of the Xinjinhe waterway and the flow guiding line connected to Longhu
352 District, Shantou City (Fig. 9 d) (Wang et al., 2017a). The other two relatively smaller
353 TMZs are distributed in the Dongxi and Waishahe estuaries, respectively. The results
354 indicate that the TMZ distribution in the HRE is mainly related to tide, runoff, estuarine
355 topography, and human activity.

356 In the MRE, the region of high TSS concentrations is mainly distributed at an
357 average distance of 1.2 km from the Yangjiang coastlines, particularly in the eastern
358 Hailingdati dike water bodies, with a mean value of more than 150 mg/L (Fig. 10a).
359 The outer shelf area has significantly lower TSS concentrations of generally less than
360 35 mg/L. The Chla concentrations in most regions of the MRE are more than 4 mg/m³,
361 except for the southwestern Dongping town coastal water bodies, where Chla
362 concentrations mainly range from 2 to 4 mg/m³. The Chla concentrations in the
363 Moyangjiang River downstream, Fuchang town coast, and outside of the Shouchanghe
364 River estuary have relatively high values of frequently greater than 8 mg/m³ (Fig. 10b).
365 Compared to the PRE and the HRE, the corresponding relationship between TSS and
366 Chla concentrations in the MRE is slightly weak. However, a trend of high (low) TSS
367 concentrations in water bodies with relatively low (high) Chla concentrations remains
368 (Figs. 10a and b).



369

370 **Fig. 10.** The estimated TSS concentrations (a), Chla concentrations (b), true color imagery (USGS
 371 1982; NASA 2001) (c), and extracted TMZ results, indicated by mango colors (d) in the MRE on
 372 December 6, 2013 (Low-flow season).

373 **Figs. 10** (c) and (d) indicate the true color imagery of the MRE and the TMZs
 374 extraction results. There are two main TMZs in the MRE on December 6, 2013. The
 375 first TMZ is mainly distributed from the inside and outside of the Moyangjiang River
 376 estuary to the Shouchanghe River estuary, with a distance of approximately 1.8 km
 377 from the coastlines (**Fig. 10d**). The distribution of TMZ in this region is mainly
 378 attributed to the interaction of tide and runoff. Another main TMZ is in the regions 4
 379 km from the Hailingdati dike, and is mainly caused by obstruction against ocean
 380 currents (**Fig. 10d**). In addition, several small, long, and narrow TMZs are accuracy
 381 extracted through TMZI with the same criterion as that in the PRE and the HRE.

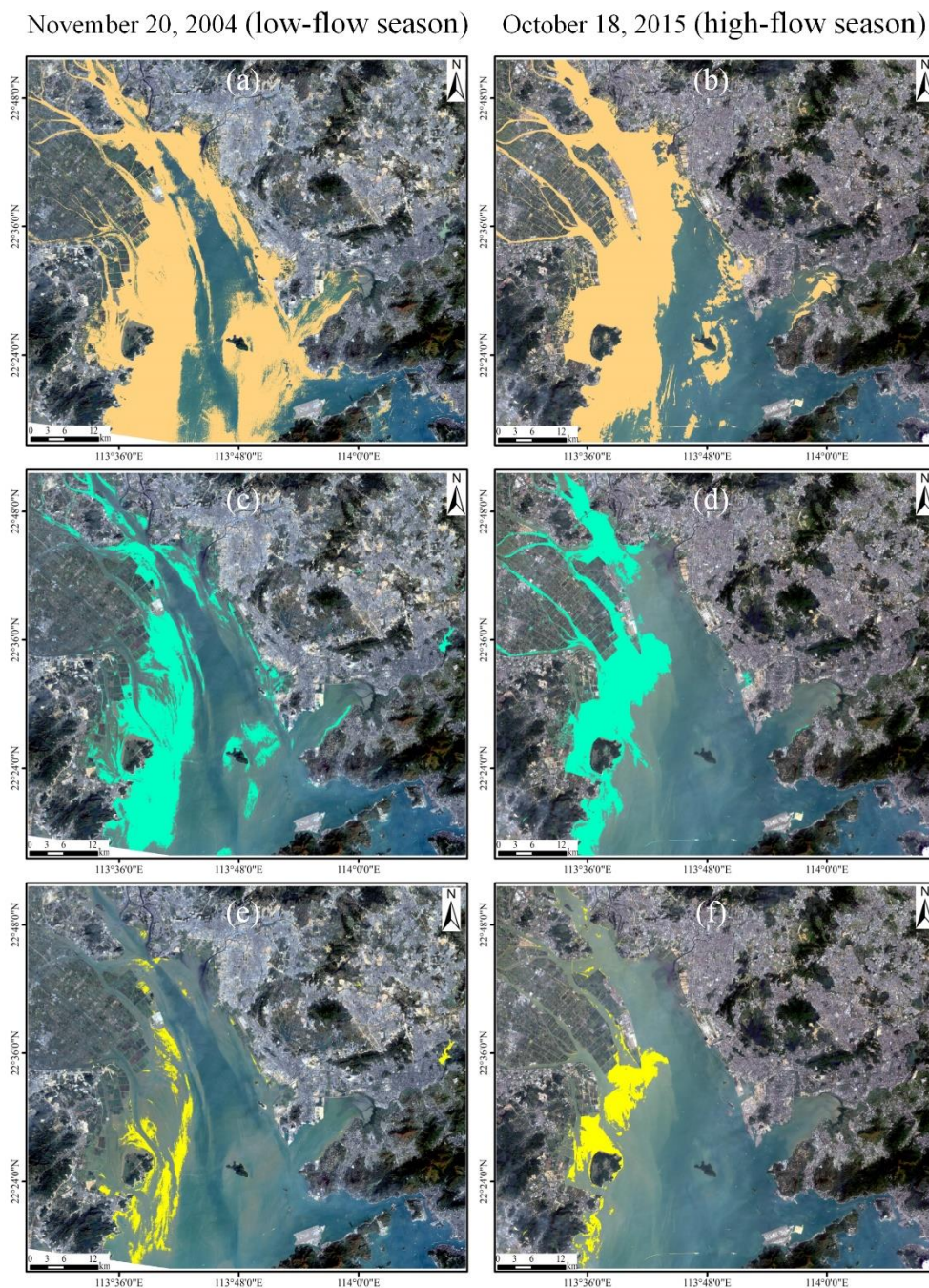
382 The results of the three estuaries and the comparison and accuracy assessment
383 indicate that extracting TMZ based on TMZI and the criterion ($TMZI > 0.2$) has a high
384 applicability in multiple estuaries and different seasons.

385 **3.5 Comparison with the previous methods**

386 Previous studies have extracted TMZ based mainly on the threshold of TSS
387 concentrations or turbidity. For example, [Jalón-Rojas et al. \(2016\)](#) used thresholds of
388 500 mg/L (300 NTU) and 1000 mg/L (600 NTU) to define moderately concentrated
389 TMZ and highly concentrated TMZ in the Loire Estuary in France; [Jiang et al. \(2013\)](#)
390 and [Li et al. \(2019\)](#) defined TMZ as the areas with TSS values larger than 700 mg/L in
391 Yangtze Estuary and Hangzhou Bay. For TMZ in the PRE, it was found that TSS values
392 in studies by [Shi et al. \(2017\)](#) and [Wai et al. \(2004\)](#) were more than 89.4 mg/L and
393 about 150 mg/L, respectively. Based on the two criteria (TMZ: $TSS > 89.4$ mg/L or
394 $TSS > 150$ mg/L), this study calculated and extracted TMZs in the PRE ([Fig. 11c-f](#)).

395 Compared to the visual interpretation TMZ results ([Figs. 7a and 8c](#)), the TMZ
396 extraction results in the PRE based on the criterion of [Shi et al. \(2017\)](#) are superior to
397 those of [Wai et al. \(2004\)](#), on November 20, 2004 ([Fig. 11c vs. Fig. 11e](#), low-flow
398 season) or October 18, 2015 ([Fig. 11d vs. Fig. 11f](#), high-flow season). The extraction
399 quality based on the criteria of [Shi et al. \(2017\)](#) and [Wai et al. \(2004\)](#) are 0.4238, 0.4770
400 and 0.1046, 0.1661, respectively. The primary reason may be that the time of the data
401 source in [Shi et al. \(2017\)](#) was closer to the present study than that in the study by [Wai](#)

402 [et al. \(2004\)](#). This means that the criterion of [Shi et al. \(2017\)](#) was more suitable for this
403 study than that of [Wai et al. \(2004\)](#).



404
405 **Fig. 11.** The true color imagery (USGS 1982; NASA 2001) and TMZ extraction results in the PRE
406 at different time (a, c, e: November 20, 2004; b, d, f: October 18, 2015) based on the TMZI method
407 of this study (a and b, regions indicated by mango color, as in [Fig. 7b](#) and [Fig. 8d](#)), the criterion by

408 [Shi et al. \(2017\)](#) (c and d, regions indicated by cyan color), and the criterion by [Wai et al. \(2004\)](#) (e
409 and f, regions indicated by yellow color).

410 It was also found that a relatively good result was obtained in the west shoal of the
411 PRE on November 20, 2004, according to the criterion of [Shi et al. \(2017\)](#) ([Fig. 11c](#)).
412 The extracted TMZs are almost consistent with the reality compared to the true color
413 imagery and the visual interpretation TMZ results ([Wang et al., 2020b, 2021](#)). However,
414 the accuracy in the east shoal and surrounding Neilingding Island of the PRE is lower
415 than in the west shoal, where obvious distributions of TMZs are not recognized
416 effectively ([Fig. 11c](#)). Furthermore, the same criterion does not work well in the western
417 shoal of the PRE at different times ([Fig. 11c](#) vs. [Fig. 11d](#)). Almost one-third of the
418 distributions of TMZs in the western shoal of the PRE during the high-flow season are
419 not distinguished and extracted ([Fig. 11d](#)). The results based on the criteria of previous
420 studies, indicate that fixed thresholds have a distinct disadvantage when extracting
421 TMZ at different times or in estuaries.

422 Based on the evaluation and analysis of all the above results ([Figs. 7-11](#)), TMZI
423 could be widely and effectively applied for the accurate extraction of estuarine TMZ,
424 regardless of the significant variations in hydrodynamic environments, TSS and Chla
425 concentrations in different estuaries and seasons. Compared to previous studies and the
426 results from fixed thresholds, it is concluded that TMZI has significant potential to
427 develop into a unified model for distinguishing and extracting TMZ effectively and
428 accurately in many other estuaries globally (Q: 0.8171-0.8429 vs. 0.1046-0.4770).

429 **4 Summary and Conclusions**

430 This study established and developed a novel model (turbidity maximum zone
431 index) based on TSS and Chla concentration, to distinguish estuarine turbidity
432 maximum zone from Landsat imageries. It was found that both TSS and Chla
433 concentrations showed significant variations and different characteristics in the PRE,
434 the HRE and the MRE in different times (Figs. 4 and 8-10). A corresponding
435 relationship between TSS and Chla concentrations in the three estuaries of Guangdong
436 Province remains. In this study, the Chla and TSS concentrations showed almost
437 opposite spatial distribution characteristics, where relatively high (low) Chla
438 concentrations corresponded exactly to the relatively low (high) TSS concentrations
439 (Figs. 4-5 and 8-10). Therefore, here, the turbidity maximum zone index (TMZI) was
440 defined and designed as the ratio of the difference and sum of the logarithmic
441 transformation of TSS and Chla concentrations.

442 Compared with the true (false) color imagery and the visual interpretation TMZ
443 results, it was found that the TMZ extraction results by TMZI were consistent with the
444 reality (Figs. 7-10; Q: 0.8171-0.8429). Notably, the criterion used for extracting TMZs
445 in different estuaries and seasons was the same ($TMZI > 0.2$). In addition, reasonable
446 accuracy and a better performance were obtained by TMZI compared with the previous
447 fixed TSS concentration or turbidity threshold (Fig. 11; Q: 0.8171-0.8429 vs. 0.1046-
448 0.4770), demonstrating that TMZI has a higher adaptability and robustness.

449 The results of this study indicate that there is significant potential for optimizing
450 TMZI to distinguish and extract TMZs from multi-source satellite remote sensing, such
451 as Sentinel, Aqua & Terra-MODIS, Envisat MERIS and SeaWiFS. This will also assist
452 in establishing and developing a global unified criterion for extracting TMZs effectively
453 in different estuaries and at different times.

454 **Code and data availability**

455 All the Landsat remote sensing imageries are fully available at
456 <https://glovis.usgs.gov/> (USGS 1982; NASA 2001).

457 **Author Contribution**

458 The individual contributions and responsibilities of the authors are listed as
459 follows: Chongyang Wang and Li Wang designed the research and wrote the paper;
460 Chenghu Zhou and Dan Li guided the research process; Danni Wang, Qiong Zheng,
461 Hao Jiang, Kai Jia and Yangxiaoyue Liu collected and analyzed the data; Shuisen Chen,
462 Ji Yang, Xia Zhou and Yong Li revised the manuscript, provided some comments and
463 helped edit the manuscript. All authors have read and agreed to the published version
464 of the manuscript.

465 **Competing interests**

466 The authors declare that they have no conflict of interest.

467 **Acknowledgements**

468 This work was funded jointly by National Natural Science Foundation of China
469 (41801364), Natural Science Foundation of Guangdong Province (2021A1515012579),
470 Key Special Project for Introduced Talents Team of Southern Marine Science and
471 Engineering Guangdong Laboratory (Guangzhou) (GML2019ZD0301), Scientific
472 Research Project approved by Department of Education of Guangdong Province
473 (2019KQNCX209), Guangdong Innovative and Entrepreneurial Research Team
474 Program (2016ZT06D336) and GDAS' Project of Science and Technology
475 Development (2020GDASYL-20200104006, 2020GDASYL-20200302001,
476 2019GDASYL-0503001, 2019GDASYL-0301001 and 2019GDASYL-0501001). We
477 would also like to thank USGS for providing the Landsat remote sensing imageries.

478 **References**

479 Asp, N.E., Gomes, V., Schettini, C.A.F., Filho, P.W.S., Siegle, E., Ogston, A.s.,
480 Nittrouer, C.A., Silva, J.N.S., Nascimento, W.R., Jr, Souza, S.R., Pereira, L.C.C.,
481 Queiroz, M.C., 2018. Sediment dynamics of a tropical tide-dominated estuary:
482 Turbidity maximum, mangroves and the role of the Amazon River sediment load.
483 Estuarine, Coastal and Shelf Science.

484 Attila, J., Kauppila, P., Kallio, K.Y., Alasalmi, H., Keto, V., Bruun, E., Koponen, S.,
485 2018. Applicability of Earth Observation chlorophyll-a data in assessment of

486 water status via MERIS-With implications for the use of OLCI sensor. Remote
487 Sensing of Environment. 212, 273-287.

488 Azhikodan, G., Yokoyama, K., 2019. Seasonal morphodynamic evolution in a
489 meandering channel of a macrotidal estuary. Science of the Total Environment.
490 684, 281-295.

491 Brenon, I., Hir, P.L., 1999. Modelling the Turbidity Maximum in the Seine Estuary
492 (France): Identification of Formation Processes. Estuarine, Coastal and Shelf
493 Science. 49, 525-544.

494 Cai, L., Shi, W., Miao, Z., & Hao, M. (2018). Accuracy Assessment Measures for
495 Object Extraction from Remote Sensing Images. Remote Sensing, 10, 303.

496 Chen, S., Fang, L., Li, H., Chen, W., Huang, W., 2011. Evaluation of a three-band
497 model for estimating chlorophyll-a concentration in tidal reaches of the Pearl River
498 Estuary, China. ISPRS Journal of Photogrammetry and Remote Sensing. 68, 356-
499 364.

500 Chen, S., Han, L., Chen, X., Li, D., Sun, L., Li, Y., 2015. Estimating wide range Total
501 Suspended Solids concentrations from MODIS 250-m imageries: An improved
502 method. ISPRS Journal of Photogrammetry and Remote Sensing. 99, 58-69.

503 Chen, X., Shen, Z., Yang, Y., 2016. Response of the turbidity maximum zone in the
504 Yangtze River Estuary due to human activities during the dry season.
505 Environmental Science and Pollution Research. 11, 1-16.

506 Feng, H., Cochran, J.K., Hirschberg, D.J., 2002. Transport and sources of metal
507 contaminants over the course of tidal cycle in the turbidity maximum zone of the
508 Hudson River estuary. *Water Research*. 36, 733-743.

509 Gebhardt, A.C., Schoster, F., Gaye-Haake, B., Beeskow, B., Rachold, V., Unger, D.,
510 Ittekkot, V., 2005. The turbidity maximum zone of the Yenisei River (Siberia) and
511 its impact on organic and inorganic proxies. *Estuarine, Coastal and Shelf Science*.
512 65, 61-73.

513 Gong, S., Gao, A., Lin, J., Zhu, X., Zhang, Y., Hou, Y., 2017. Temporal-spatial
514 distribution and its influencing factors of suspended particulate matters in
515 Minjiang lower reaches and estuary. *Journal of Earth Sciences and Environment*.
516 39(6), 826-836.

517 Grasso, F., Verney, R., Hir, P.L., Thouvenin, B., Schulz, E., Kervella, Y., Fard, I.K.P.,
518 Lemoine, J.-P., Dumas, F., Garnie, V., 2018. Suspended Sediment Dynamics in the
519 Macrotidal Seine Estuary (France) - Part 1: Numerical Modeling of Turbidity
520 Maximum Dynamics. *Journal of Geophysical Research: Oceans*. 123, 558-577.

521 Gregg, W.W., Casey, N.W., 2004. Global and regional evaluation of the SeaWiFS
522 chlorophyll data set. *Remote Sensing of Environment*. 93, 463-479.

523 Huang, B., Hong, H., Ke, L., Cao, Z., 2005. Size-fractionated phytoplankton biomass
524 and productivity in the Zhujiang River Estuary in China. *Acta Oceanologica Sinica*.
525 27, 180-186.

526 Jalón-Rojas, I., Schmidt, S., Sottolichio, A., Bertier, C., 2016. Tracking the turbidity
527 maximum zone in the Loire Estuary (France) based on a long-term, high-
528 resolution and high-frequency monitoring network. *Continental Shelf Research*.
529 117, 1-11.

530 Jiang, J., He, Q., Zhu, L., Lin, J., 2019. Analysis of hydrodynamic features of the North
531 Passage in the turbidity maximum, Changjinag Estuary. *Haiyang Xuebo*. 41(1),
532 11-20.

533 Jiang, X., Lu, B., He, Y., 2013. Response of the turbidity maximum zone to fluctuations
534 in sediment discharge from river to estuary in the Changjiang Estuary (China).
535 *Estuarine, Coastal and Shelf Science*. 131, 24-30.

536 Kim, H.H., Ko, B.C., Nam, J.Y., 2016a. Predicting chlorophyll-a using Landsat 8 OLI
537 sensor data and the non-linear RANSAC method –a case study of Nakdong River,
538 South Korea. *International Journal of Remote Sensing*. 37, 3255-3271.

539 Kim, W., Moon, J.-E., Park, Y.-J., Ishizaka, J., 2016b. Evaluation of chlorophyll
540 retrievals from Geostationary Ocean Color Imager (GOCI) for the North-East
541 Asian region. *Remote Sensing of Environment*. 184, 482-495.

542 Kitheka, J.U., Mavuti, K.M., Nthenge, P., Obiero, M., 2016. The turbidity maximum
543 zone in a shallow, well-flushed Sabaki estuary in Kenya. *Journal of Sea Research*.
544 110, 17-28.

545 Le, C., Hu, C., Cannizzaro, J., English, D., Muller-Karger, F., Lee, Z., 2013. Evaluation
546 of chlorophyll-a remote sensing algorithms for an optically complex estuary.
547 Remote Sensing of Environment. 129, 75-89.

548 Le, C., Li, Y., Zha, Y., Sun, D., Huang, C., Lu, H., 2009. A four-band semi-analytical
549 model for estimating chlorophyll a in highly turbid lakes: The case of Taihu Lake,
550 China. Remote Sensing of Environment. 113, 1175-1182.

551 Li, L., Ye, T., Wang, X., Xia, Y., 2019. Tracking the multidecadal variability of the
552 surface turbidity maximum zone in Hangzhou Bay, China. International Journal of
553 Remote Sensing. 1-22.

554 Liu, H., Huang, L., Tan, Y., Ke, Z., Liu, J., Zhao, C., Wang, J., 2017. Seasonal variations
555 of chlorophyll a and primary production and their influencing factors in the Pearl
556 River Estuary. Journal of Tropical Oceanography. 36, 81-91.

557 Liu, R., Wang, Y., Gao, J., Wu, Z., Guan, W., 2016. Turbidity maximum formation and
558 its seasonal variations in the Zhujiang (Pearl River) Estuary, southern China. Acta
559 Oceanologica Sinica. 35, 22-31.

560 Mitchell, S., 2013. Turbidity maxima in four macrotidal estuaries. Ocean & Coastal
561 Management. 79, 62-69.

562 Mitchell, S., Akesson, L., Uncles, R., 2012. Observations of turbidity in the Thames
563 Estuary, United Kingdom. Water and Environment Journal. 26, 511-520.

564 Montanher, O., Novo, E., Barbosa, C., Renno, C., Silva, T., 2014. Empirical models for
565 estimating the suspended sediment concentration in Amazonian white water rivers

566 using Landsat 5/TM. International Journal of Applied Earth Observation and
567 Geoinformation, 29, 67-77.

568 Park, K., Wang, H.V., Kim, S.-C., Oh, J.-H., 2008. A Model Study of the Estuarine
569 Turbidity Maximum along the Main Channel of the Upper Chesapeake Bay.
570 Estuaries and Coasts. 31, 115-133.

571 Pozdnyakov, D., Shuchman, R., Korosov, A., Hatt, C., 2005. Operational algorithm for
572 the retrieval of water quality in the Great Lakes. Remote Sensing of Environment.
573 97, 352-370.

574 Schubel, J., 1968. Turbidity maximum of the northern chesapeake bay. SCIENCE. 161,
575 1013-1015.

576 Shen, H., 1995. New understanding on the study of the maximum turbidity zone in
577 estuaries of China. Advence in Earth Sciences. 10, 210-212.

578 Shen, H., He, S., Mao, Z., Li, J., 2001. On the turbidity maximum in the Chinese
579 estuaries. Journal of Sediment Research. 1, 23-29.

580 Shi, W., Shen, H., Li, J., 1993. Review on the formation of estuarine turbidity maximum.
581 Advence in Earth Sciences. 8, 8-13.

582 Shi, Z., Xu, J., Huang, X., Zhang, X., Jiang, Z., Ye, F., Liang, X., 2017. Relationship
583 between nutrients and plankton biomass in the turbidity maximum zone of the
584 Pearl River Estuary. Journal of Environmental Sciences. 57, 72-84.

585 Song, K., Li, L., Tedesco, L.P., Li, S., Duan, H., Liu, D., Hall, B.E., Du, J., Li, Z., Shi,
586 K., Zhao, Y., 2013. Remote estimation of chlorophyll-a in turbid inland waters:

587 Three-band model versus GA-PLS model. *Remote Sensing of Environment*. 136,
588 342-357.

589 Toublanc, F., Brenon, I., Coulombier, T., 2016. Formation and structure of the turbidity
590 maximum in the macrotidal Charente estuary (France)_ Influence of fluvial and
591 tidal forcing. *Estuarine, Coastal and Shelf Science*. 169, 1-14.

592 Uncles, R.J., Bloomer, N.J., Frickers, P.E., Griffiths, M.L., Harris, C., Howland, R.J.M.,
593 Morris, A.W., Plummer, D.H., Tappin, A.D., 2000. Seasonal variability of salinity,
594 temperature, turbidity and suspended chlorophyll in the Tweed Estuary. *The*
595 *Science of the Total Environment*. 251/252, 115-124.

596 Wai, O.W.H., Wang, C.H., Li, Y.S., Li, X.D., 2004. The formation mechanisms of
597 turbidity maximum in the Pearl River estuary, China. *Marine Pollution Bulletin*.
598 48, 441-448.

599 Wan, Y., Wang, L., 2017. Numerical investigation of the factors influencing the vertical
600 profiles of current, salinity, and SSC with in a turbidity maximum zone.
601 *International Journal of Sediment Research*. 32, 20-33.

602 Wang, C., Chen, S., Li, D., Wang, D., liu, W., Yang, J., 2017a. A Landsat-based model
603 for retrieving total suspended solids concentration of estuaries and coasts in China.
604 *Geoscientific Model Development*. 10, 4347-4365.

605 Wang, C., Chen, S., Yang, J., Li, Y., Zhou, X., Li, D., Wang, D., 2020a. Monitoring total
606 suspended solids concentrations in estuaries based on remote sensing. Beijing:
607 China Water & Power Press.

608 Wang, C., Li, D., Wang, D., Chen, S., 2017b. Detecting the Temporal and Spatial
609 Changes of Suspended Sediment Concentration in Hanjiang River Estuary During
610 the Past 30 Years Using Landsat Imageries. *Research Journal of Environmental*
611 *Science*. 11, 143-155.

612 Wang, C., Li, W., Chen, S., Li, D., Wang, D., Liu, J., 2018. The spatial and temporal
613 variation of total suspended solid concentration in Pearl River Estuary during
614 1987–2015 based on remote sensing. *Science of the Total Environment*. 618, 1125-
615 1138.

616 Wang, C., Wang, D., Yang, J., Fu, S., Li, D., 2020b. Suspended Sediment within
617 Estuaries and along Coasts: A Review of Spatial and Temporal Variations based
618 on Remote Sensing. *Journal of Coastal Research*. 36, 1323-1331.

619 Wang, C., Zhou, C., Chen, S., Xie, Y., Li, D., Yang, J., Zhou, X., Li, Y., Wang, D., Liu,
620 Y., 2021. Retrospect and perspective of the estuarine turbidity maximum zone
621 researches. *Chinese Science Bulletin*. 66, 2328-2342.

622 Yan, D., Song, D., Bao, X., 2020. Spring-neap tidal variation and mechanism analysis
623 of the maximum turbidity in the Pearl River Estuary during flood season. *Journal*
624 *of Tropical Oceanography*. 39, 20-35.

625 Yang, J., Liu, W., 2015. Characteristics of the maximum turbidity zone in the
626 lingdingyang-Pearl river estuary during the flood season in the recent 30 years.
627 *Pearl River Water Transport*. 16, 58-62.

- 628 Yang, Y., Li, Y., Sun, Z., Fan, Y., 2014. Suspended sediment load in the turbidity
629 maximum zone at the Yangtze River Estuary: The trends and causes. *Journal of*
630 *Geographical Sciences*. 24, 129-142.
- 631 Yu, Q., Wang, Y., Gao, J., Gao, S., Flemming, B., 2014. Turbidity maximum formation
632 in a well-mixed macrotidal estuary: The role of tidal pumping. *Journal of*
633 *Geophysical Research: Oceans*. 119, 7705-7724.
- 634 Zhang, X., Chen, X., Dou, X., Zhao, X., Xia, W., Jiao, J., Xu, H., 2019. Study on
635 formation mechanism of turbidity maximum zone and numerical simulations in
636 the macro tidal estuaries. *Advances in Water Science*. 30, 84-92.